WU Mengwen[1,2], DONG Meiying[1], CHEN Feng[1,*]

[1]Zhejiang Institute of Meteorological Sciences, Hangzhou 310008, P. R. China

[2]State Key Laboratory of Severe Weather, Chinese Academy of Meteorological Sciences, Beijing 100081

Submitted to ***JGR-Atmoshpere***

Key Points:

- The ensemble approach is more valuable for forecasting precipitation than for forecasting temperature, mixing ratio, and wind speed
- The individual impacts of urban canopy parameters have different sensitivity to different meteorological variables
- Urbanization increases the area with a probability of high temperature, low mixing ratio, low wind speed, and extreme precipitation

Abstract

The urban morphology determined by urban canopy parameters (UCPs) plays an important role in simulating the interaction of urban land surface and atmosphere. The impact of urbanization on a typical summer rainfall event in Hangzhou, China, is investigated using the integrated WRF/urban modelling system. Three groups of numerical experiments are designed to assess the uncertainty in parameterization schemes, the sensitivity of urban canopy parameters (UCPs), and the individual and combined impacts of thermal and dynamical effects of urbanization, respectively. The results suggest that the microphysics scheme has the highest level of uncertainty in simulating precipitation, followed by the planetary boundary layer scheme, whereas the land surface and urban physics schemes have minimal impacts. The choices of the physical parameterization schemes for simulating precipitation are much more sensitive than those for simulating temperature, mixing ratio, and wind speed. Of the eight selected UCPs, changes in heat capacity, thermal conductivity, surface albedo, and roughness length have a greater impact on temperature, mixing ratio, and precipitation, while changes in building height, roof width, and road width affect the wind speed more. The total urban impact could lead to higher temperature, less mixing ratio, lower wind speed, and more precipitation in and around the urban area. Comparing the thermal and dynamical effects of urbanization separately, both of them contribute to an increase in temperature and precipitation and the thermal effect plays a major role. However, their impacts are opposite in changes of mixing ratio and wind speed and each play a major role respectively.

Plain language summary

Limited knowledge exists over how factors related to urbanization affect local short-term precipitation in cities, which is a common precipitation type but difficult to forecast. In this study, a typical summer heavy precipitation event occurred in Hangzhou, China is chosen to analyze the urban effect using both ensemble simulation method and sensitivity test method. The ensemble simulation can well reproduce the heavy precipitation and the high temperature, low mixing ratio, and weak wind speed before precipitation in the urban area. The performance of the model is shown to have more uncertainties in forecasting precipitation than the uncertainties in temperature, mixing ratio, and wind speed. The thermal and dynamic effects of urbanization on this rainfall event are further separated and compared. Both the thermal and dynamic effects contribute to an increase in temperature and precipitation in the urban area. However, they play the opposite role in the changes of mixing ratio and wind speed. The thermal effect plays a major role and decrease the mixing ratio, and the dynamical effect is dominant on changes in wind speed and reduces the wind speed.

Keywords: urbanization effect, urban canopy parameter, ensemble simulation

1 Introduction

The rapid urbanization of China, which involves population aggregation and impervious surface expansion, has artificially changed the land cover and physical properties of land surface. This has led to a series of climate and environmental issues, such as the urban heat islands (UHIs) Portman 1993Ren et al. 2008Yang et al. 2011a(; ;), extreme rainfall Jiang et al. 2020Wen et al. 2020Zhang et al. 2009(; ;), and air pollution Wang et al. 2007Zhang et al. 2016(;). To address these urban environmental issues, an integrated urban modelling system is coupled to the Weather Research and Forecasting (WRF) model to bridge the gaps between traditional mesoscale modelling and microscale modelling Chen et al. 2022bHe et al. 2019Miao et al. 2015Shen et al. 2019Shui et al. 2016(; ; ; ;) Three urban parameterization schemes, i.e., bulk parameterization Liu et al. 2006(), the single-layer urban canopy model (SLUCM) Kusaka and Kimura 2004Kusaka et al. 2001(;), and the building effect parameterization (BEP) Martilli et al. 2002(), with different degrees of freedom to parameterize urban surface processes, are used to analyze how urban morphology and its thermal and dynamical effects influence the local micrometeorology.

In general, urbanization can produce less evaporation, higher surface temperature, larger thermal transport (sensible and latent heating), and a deeper boundary layer (Chen et al. 2022b; Shui et al. 2016; Zhang et al. 2009). Chen et al. (2016) indicated that the anthropogenic heat release in Hangzhou, China, contributed 65.26% and 17.47% to the UHI intensity in winter and summer, respectively. Both the high-rise buildings and the UHI-induced

circulation (Fujibe 2003) modifies the 10-m wind fields, for example, reducing the regional wind speed and causing a weak wind zone in the urban areasMittal et al. 2018(). Furthermore, numerous studies consistently found urbanization increases in the amount and frequency of extreme precipitation over and downwind of cities (Zhang 2020; Wu et al. 2019; Wan et al. 2015; Miao et al. 2011). However, the uncertainty in forecasting precipitation is usually much larger than the uncertainties in temperature and wind field. In this case, ensemble forecast is more credible for studying the urban effect on extreme precipitation than a single model run (Schwartz et al. 2014). Studies of urban impact on rainfall without ensemble runs probably overestimate urbanization effects on rainfall, sometimes up to 100% (Berner et al. 2011; Yu et al. 2018).

In addition, the urban morphology determined by urban canopy parameters (UCPs) that used to drive these processes also can greatly affect the thermal and dynamical fields in the urban areas Chen and Ng 2011Martilli 2007(;). Zhou and Chen (2018) indicated that the increasing building height may mitigate the UHI intensity at the pedestrian level due to the shading effects of high-rise buildings. Many urban greening and white roof experiments showed that the surface temperature and UHI were reduced obviously due to the surface albedo changed Akbari et al. 1992Coutts et al. 2013Liu et al. 2018Millstein and Menon 2011Smith and Roebber 2011(; ; ; ;). Three dimensional UCPs datasets were developed both in the United States Ching et al. 2009() and China Sun et al. 2021(), with which the model skill in simulating 2-m temperature and 10-m wind speed was greatly improved He et al. 2019Ronda et al. 2017(;). Besides, Shen et al. (2019) found that the impact of updating urban fraction and urban morphology were obvious on wind speed but minor on temperature and humidity in Guangzhou, China. However, these studies mainly focus on the impact of changes in either a single UCP or the entire UCPs dataset on the urban environment, a diagnostic analysis of isolating the contributions of these UCPs on the thermal and dynamic fields has been less conducted.

In this study, the individual and combined impacts of thermal and dynamical effects of urbanization are investigated through several sensitivity experiments. A typical summer rainfall event occurred under a weak synoptic forcing background in Hangzhou, China is chosen. Hangzhou is one of the central cities in the Hangzhou Bay with a permanent population of 12.2 million in 2021 (Zhejiang Statistical Bureau; http://tjj.zj.gov.cn/col/col1525563/index.html), and has experienced rapid economic development and urbanization in the past two decades. Analysis of the remote sensing night light data shows that the urban distribution in the Hangzhou Bay area has developed from a point-like distribution in the 1990s to a continuous belt-like distribution nowadays, and the urban area has increased by more than three times Yang et al. 2015(). Wide roads and high-rise buildings rise in Hangzhou megacity, which changes the physical properties of the underlying surface and has a great impact on the urban environment. Thus, it is necessary to investigate the urban effects on the local micrometeorology of Hangzhou and, in turn, to improve the understanding of the interaction mechanism of urban land surface and atmosphere.

The paper is organized as follows: the description of the study area, synoptic background, model configuration, and simulation experiments are given in section 2. Section 3 evaluates the performance of the model, and discusses the impacts of UCPs as well as the thermal and dynamical effects of urbanization on this rainfall event. The paper ends with a summary of the main findings in section 4.

2 Methodology

2.1 Synoptic background

The selected summer rainfall case occurred between 13:00 to 16:00 BST on 26 July 2018, with a maximum hourly rainfall amount exceeding 114.7 mm at Liancheng Station (30.367°N, 120.283°E) near the downtown of Hangzhou. Before and during this event, Hangzhou is dominated by the uniform west Pacific subtropical high-pressure system with relatively weak winds and less favorable moisture conditions (Fig. 1). Moreover, high temperature phenomena (35 °C at 10:00 BST) is observed in Hangzhou before the precipitation. This synoptic pattern is not conductive to form regional rainfall but is favorable to initiate local rainfall. Therefore, this case is suitable to study the impacts of urban thermal and dynamical effect on the simulation of local heavy precipitation and the high temperature before. Hereafter, our entire study period is from 09:00 to 18:00 BST on July 26, 2018.

2.2 Model configuration

The model used in the current study is the WRF-ARW coupled with urban model version 4.0.2 (http://www2.mmm.ucar.edu/wrf/users), which is widely used for mesoscale numerical simulation research in the world Skamarock et al. 2019(). Figure 2a shows the terrain of our study area and the location of Hangzhou. All the simulations have two one-way nested domains centered at (31.0°N, 120.5 °E) with a horizontal grid spacing (grid numbers) of 4 km (353 × 403) and 1 km (457 × 413), respectively. The vertical coordinate contains 51 full sigma levels from surface to 10 hPa. Approximately eight of these levels are designed below 1 km to provide a fine vertical resolution within the planetary boundary layer, and the lowest half-sigma level height is approximately 35 m above ground. The black rectangle box (119.9-120.8 °E, 29.8-30.7 °N) in Fig.2b is referred to as the control region in this study as the urban area and heavy precipitation are concentrated in this region.

To assess contributions of model physics parameterizations to biases in simulations of this local heavy rainfall event, two types of land surface, i.e., Noah Tewari et al. 2016() and NoahMP Niu et al. 2011Yang et al. 2011b(;), two types of urban surface, i.e., SLUCM Chen et al. 2011() and BEP Martilli et al. 2002(), three types of microphysics, i.e., Purdue Lin Chen and Sun 2002(), WSM6 Hong and Lim 2006(), and WDM6 Lim and Hong 2010(), and two types of planetary

boundary layer, i.e., MYJ Janjić 1994Mesinger 1993(;), and Boulac Bougeault and Lacarrere 1989(), are chosen for the physical parameterization perturbations of the ensemble forecast in this study. In addition, the RRTMG Iacono et al. 2008() is employed for both shortwave and longwave radiation schemes in the simulation. No cumulus parameterization is used as recommended in the paper of Skamarock et al. (2019), given that the model can resolve the deep convective updrafts itself. All the physical schemes used are identical for both two nests. The description of the model configuration is summarized in Table 1.

Considering the rapid urban expansion in and around Hangzhou, the default MODIS 20-category land use dataset Strahler 1999() used in our study is updated by a more inhomogeneous and detailed urban land cover and fraction dataset at 1 km $\times$ 1 km resolution Chen et al. 2014(). Using this dataset has been proved to better simulate the UHIs Chen et al. 2014Chen et al. 2016(;) and extreme rainfall Chen et al. 2022a() in Hangzhou. For more descriptions of this dataset, see Chen et al. (2014).The updated land use map is shown in Figure 2b, and the Hangzhou-Shaoxing mega city with an urban fraction 0.2 is highlighted with the magenta solid line.

2.3 Numerical experiment design

Three groups of numerical experiments, i.e., GROUP I, II, and III, are designed in our study (Table 2). In GROUP I, there are a total of 24 ensemble members with the same model configurations except for different combinations of physical parameterization schemes. Every ensemble member is named by the option of the selected physical parameterization schemes, e.g., the name of "m2p2s2u1" represents that Lin(2), MYJ(2), Noah(2), and SLUCM(1) are selected for the microphysics, PBL physics, land surface, and urban physics schemes of this ensemble member, respectively. The control ensemble forecast (ENCTL) includes these 24 members running with the real land use data. Another ensemble forecast (referred to as ENNoUB) is designed the same as the ENCTL, but replace the urban land use with cropland in each member to investigate the impact of urbanization. In GROUP II, one control simulation called CTL (the member of "m16p8s4u2" in ENCTL) and another 16 sensitivity tests (i.e., SEN1, SEN2, ..., and SEN16) are conducted to systematically explore the effects of UCPs to the simulation of urban environment. Each sensitivity test is the same as the CTL, but decrease or increase one UCP (such as the building height) by 50%. In GROUP III, another 3 sensitivity tests (referred to as NOTH, NODY, and NOUB) are conducted and compared to the CTL to investigate the thermal and dynamical effects of urbanization. The NOTH, NODY, and NOUB run are designed the same as the CTL, but artificially remove the urban thermal effect, urban dynamical effect, and both of them, respectively. The urban process, as a part of the land surface process, influences the bottom boundary variables in WRF following Eq. (1).

$$V_{\text{grid}} = V_{\text{veg}} \times (1 - w_{\text{urb}}) + V_{\text{urb}} \times w_{\text{urb}} \quad (1)$$

where V_{grid} is the variable (e.g., surface temperature, sensible heat flux, and friction velocity) from the surface to the lowest layer of the grid; V_{veg} is the same variable from the land surface model for the natural vegetation surfaces; V_{urb} is the same variable from the urban canopy model for the artificial surfaces; and w_{urb} is the fraction coverage of artificial surfaces. The urban thermal effect is removed by setting $w_{\text{urb}} = 0$ for the thermal related variables, including albedo, surface temperature, sensible heat flux, latent heat flux, and ground heat flux. The dynamical effect is removed by setting $w_{\text{urb}} = 0$ for the dynamical related variables including friction velocity and momentum.

All the simulations are initialized at 02 BST on July 26, 2018, and integrated for 18 hours. The hourly ERA5 reanalysis data Hersbach et al. 2018() with a resolution of 0.25°×0.25° is used to provide the initial and lateral boundary conditions. No data assimilation or nudging is performed to avoid the influence of other factors.

The meteorological variables, including precipitation, 2-m temperature (T2M), 2-m mixing ratio (Q2M), and 10-m wind speed (WS10M), are derived from the minute-level surface observations maintained by the Zhejiang Meteorological Bureau, China Meteorological Administration. The gauged variables are interpolated into the model grid by using the inverse distance weighted method. This interpolation method has been proved to be insensitive to the results Ikeda et al. 2010Xu et al. 2017(;). Thus, the gridded observation data are used for a quantitative evaluation of the model performance. To avoid the disturbance of precipitation, the thermal related variables (i.e., surface temperature, T2M, Q2M, sensible heat flux, latent heat flux, ground heat flux, and net radiation flux) are calculated before precipitation (i.e., from 10:00 to 13:00 BST on 26 July 2018), while the other variables are calculated during the entire study period (i.e., from 10:00 to 18:00 BST on 26 July 2018).

3 Results

3.1 Evaluation of WRF simulation

The accumulated precipitation from 13:00 to 18:00 BST on July 2018 is simulated by 24 ensemble tests with different combination of physical schemes using a map of current land use (ENCTL in Group I). The threat score (TS) is used to evaluate the performance of each test in predicting the accumulated precipitation (Table 3). The TS is defined as:

$TS = \frac{N_a}{N_t - N_b}$ (2)

where N_a is the number of simulations that capture the observation, N_b is the number of missing grids, and N_t is the number of total grids.

The performance of the model in capturing the occurrence of rainfall (0.1 mm) is generally good, with the averaged TS >0.85 accuracy, although the model performance gradually decreases at higher accumulations. Only 3 of the 24

members have TS >0.1 when the precipitation is >50 mm. Comparing the TS among all the members in each category (0.1, 10, 25, and 50 mm), the microphysics scheme plays a key part in forecasting rainfall and the majority of the members with higher TS use the microphysics scheme of WDM6 (16). A combination of the WDM6 (16), BouLac (8), Noah MP (4), and BEP (2), i.e., m16p8s4u2, gets the highest TS when precipitation is 10 and 25 mm, and gets the second highest TS when precipitation is 0.1 mm. The composite radar reflectivity simulated by m16p8s4u2 is compared with the observation in Figure 3. The model successfully captures the first well defined radar echo formed in the southeast corner of the control region at 14:00 BST on 26 July 2018, except for about 1.5 h early (Fig. 3a1 vs. 3a2). Then the convective system moves northwestward with a rapid intensification in the next two hours (Fig. 3b1-3b2). The radar echo reaches its maximum value at 16:00 BST in the urban area of Hangzhou, which is also well simulated by the CTL with an approximate shift of 1.5 h in advance (Figure 3c1-3c2). After 16:00 BST, the convective system gradually weakens and moves out of the study area (Fig. 3d1-3d2). In general, the m16p8s4u2 successfully captures the evolution of the heavy-rain-producing convective system and is chosen as the CTL.

The averaged T2M, Q2M, and WS10M before precipitation (from 10:00 to 13:00 BST on 26 July 2018), and the accumulated precipitation (from 13:00 to 18:00 BST on 26 July 2018) of the ENCTL are both qualitatively (Fig. 4) and quantitatively (Table 4) compared with the observations. The deviation (BIAS) and root-mean-square error (RMSE) based on the following definitions are used to analyze the averaged uncertainty of the four meteorological variables.

$$\mathrm{BIAS} = \frac{1}{N}\sum_{i=1}^{N}(X_i - Y_i), \quad (3)$$

$$\mathrm{RMSE} = \frac{1}{N}\sum_{i=1}^{N}(X_i - Y_i)^2, \quad (4)$$

where X_i and Y_i represent the variable in each grid from WRF model and observation, respectively, and $\overline{X}$ and $\overline{Y}$ are their corresponding mean values.

Under the influence of the subtropical high, Hangzhou is sunny and hot before precipitation. The observed temperature reaches 38 °C in the urban area of the control region, which shows a clear UHI phenomenon (Fig. 4a1). Compared with the observation, the ENCTL well captures the main features of T2M with slight underestimation (Fig. 4b1), and the CTL successfully reports an extremely high temperature of 39 °C in the urban area (Fig. 4c1). The spread of T2M is small in the ENCTL (Fig. 4d1), indicating that the high temperature and the UHI are well reproduced by most members. Accompanied by the hot weather, Hangzhou is also characterized by low moisture (Fig. 4a2) and small wind speed (Fig. 4a3). Both the ensemble means of the ENCTL and the CTL capture these features, i.e., relatively smaller values of Q2M (Fig. 4b2, 4c2) and WS10M (Fig. 4b3, 4c3) within the control region than those outside the control region. These scenarios, known as the urban heat island, dry island, and turbid island (exacerbated by low wind speed), are similar to those shown by previous studies Chen and Jiang 2006Miao et al. 2009Shen et al. 2019Wang and Gong

2010(; ; ;).

The accumulated precipitation is mainly concentrated in the control region (Fig. 4a4). The CTL well reproduces the spatial distribution and magnitude of the accumulated precipitation (Fig. 4c4). In the ensemble mean of the ENCTL, although a large value center could be found inside the control region, the rainfall magnitude is much underestimated and the center shift about 35 km to the east (Fig. 4b4). This is consistent with previous findings that some signals of extreme rainfall may be weakened by the ensemble meanYu et al. 2018(). It should be noted that the spread of precipitation is much larger inside the control region, indicating that there are more uncertainties in forecasting precipitation inside the urban area than that in the natural land use (Fig. 4d4).

Compared to the magnitude of the ensemble means, the variations of BIAS and RMSE are relatively small in T2M, Q2M, and WS10M than those in precipitation, which suggests that the uncertainty of forecasting precipitation is much larger than the uncertainties in T2M, Q2M, and WS10M (Table 4). The performance of the model in forecasting the last three variables could be less improved by changing the options of various physical schemes, but quite valuable for forecasting short-term local heavy rainfall.

A comparison of the hourly variations of averaged T2M, Q2M, WS10M, and precipitation between the observed and the ENCTL suggests that most of the members well capture the evolution of this event (Fig. 5). However, the T2M drops faster during the precipitation period and then keeps in a higher level afterwards in the ENCTL than observation (Fig.5a). Besides, most of the members underestimate the Q2M (Fig. 5b) but overestimate the WS10M (Fig. 5c) during the entire study period. Finally, similar to CTL, the precipitation starts 1-2 h earlier in most members (Fig. 5d). The premature estimates of the convective initialization may be a common difficulty in simulating local convection.

In general, the uncertainties in forecasting T2M, Q2M, and WS10M are smaller than the uncertainty in precipitation. The uncertainty in forecasting precipitation is much larger in the urban area than that in the surrounding nonurban area. A comparison of the parameterization schemes suggests that microphysics scheme plays the most important role in forecasting precipitation, followed by the PBL, whereas the land surface and urban physics schemes have minimal impacts. This result is consistent with the work of Yu et al. (2018) and Chen et al. (2022a), who also indicated that the microphysics and PBL schemes can substantially affect the temperature and moisture profiles in the lower troposphere, and then have a significant impact on precipitation simulation.

3.2 Sensitivity analysis of urban canopy parameters

Previous researches indicate that urban morphology determined by UCPs has a great impact on the numerical simulation of urban environment He et al. 2019Kusaka and Kimura 2004Miao et al. 2009Shen et al. 2019Sun et al. 2021(; ; ; ;). Eight most important parameters for characterizing urban canopy (i.e.,

building height, roof width, road width, anthropogenic heat, heat capacity, thermal conductivity, surface albedo, and roughness length) are selected and increased/decreased by 50% to investigate their individual sensitivity on T2M (Fig. 6), Q2M (Fig. 7), WS10M (Fig. 8), and accumulated precipitation (Fig. 9), respectively. To avoid the disturbance of precipitation, the first three variables at 10:00 BST and the 1-hr accumulated precipitation during 13:00-14:00 BST are chosen for comparing the impacts of UCPs. One common feature is that the influences of UCPs on simulated meteorological elements are concentrated in the urban area. Changes in WS10M and precipitation are less obvious than those in the T2M and Q2M, because they involve more complicated mechanisms, especially the precipitation processes Huang et al. 2019Yin et al. 2020(;).

For changes in T2M (Fig.6), UCPs of building height, heat capacity, thermal conductivity, and surface albedo have a negative feedback effect, while the other four UCPs have a positive feedback effect. Considering the magnitude of temperature change, the impacts of heat capacity, thermal conductivity, surface albedo, and roughness length (Fig. 6i-6p) are more obvious than the impacts of building height, roof width, road width, and anthropogenic heat (Fig. 6a-6h). The temperature decreases by about 0.05-0.2 °C in the urban area by increasing the heat capacity, thermal conductivity, or surface albedo, and increases by 0.04-0.08 °C by increasing the roughness length. Compared with the changes above, differences in T2M are much smaller by changing the building height, roof width, road width, or anthropogenic heat. The effects of UCPs on Q2M (Fig. 7) are opposite to those on T2M, except for changes in the building height. This is also consistent with previous findings that the increase of temperature in the urban area would enhance the ground evaporation and leads to a smaller mixing ratio Zhang et al. 2009(). For changes in WS10M (Fig.8), UCPs of the building height, heat capacity, thermal conductivity, and surface albedo have a negative feedback effect, while roof width, roughness length, and road width have a positive feedback effect. The anthropogenic heat has a negligible effect on the changes of WS10M. The influences of UCPs on precipitation (Fig. 9), however, is less uniformly distributed than those on the other three meteorological elements. Both positive and negative feedback effects can be observed in the urban area, suggesting large uncertainties in forecasting heavy precipitation there. Similar to T2M and Q2M, the impacts of heat capacity, thermal conductivity, surface albedo, and roughness length on precipitation (Fig. 9i-9p) are more obvious than the impacts of the other four UCPs (Fig. 9a-9h). In general, the simulations of T2M, Q2M, and precipitation are more sensitive to the heat capacity, thermal conductivity, surface albedo, while the simulation of WS10M is more sensitive to the building height, roof width, and road width.

Figure 10 lists the differences of multiple meteorological variables averaged in the control region when increasing the values of the eight UCPs by 50% individually. Firstly, consistent with the finding above, both T2M and Q2M are more sensitive to changes in heat capacity, thermal conductivity, surface albedo, and roughness length. The WS10M is mainly affected by the structural parameters

(i.e., building height, roof width, and road width). As the effect of UCPs on precipitation is not evenly distributed in space, the conclusion made by the region averaged values is less consistent with that in Figure 9.

The influences of UCPs on more meteorological variables are also examined. The surface albedo, building height, roof width, and road width play an important role in the urban canopy radiation balance, i.e., changes in downward/upward shortwave (SWDOWN/SWUP). The surface albedo, which quantifies the fraction of the sunlight reflected by the surface of the earth, is the parameter that has the greatest impact on most of the meteorological variables. The increase of surface albedo reflects more shortwave radiation and reduces net shortwave radiation (NSW) entering the urban canopy, which leads to a decrease in both surface temperature (TSK) and T2M. Although more NSW is trapped as the building height increases, less energy reaches the surface ground and the TSK decreases due to the longer building shadow. The temperature gradient in the canopy also increases and causes more energy to be transported into the ground (GRDFLX), resulting in a decrease in T2M. The opposite phenomenon could be found when increasing the roof width and road width, which leads to an increase in both TSK and T2M. On the other side, the heat capacity and thermal conductivity have a great influence on the surface energy balance, i.e., changes in sensible heat flux (HFX) and ground heat flux (GRDFLX). The increases of heat capacity and thermal conductivity mean that the building could store more energy in the urban canopy and conduct it into the ground, therefore causing a decrease in T2M. The increase of roughness length enhances the mixing capacity of the boundary layer, and more heat is conducted to the upper boundary layer during the daytime, resulting in an increase in GRDFLX and a decrease in TSK. The anthropogenic heat is treated as an additional sensible heat source in the model and leads to a higher temperature and a larger HFX, although its impact is relatively small compared to the other UCPs.

3.3 Impacts of the thermal and dynamical effects of urbanization

The impact of urbanization is examined by comparing the differences in T2M, Q2M, WS10M, and accumulated precipitation between ENCTL and ENNoUB (Fig. 11). The increase in the ensemble mean of T2M is 0.4-1.2 ^{o}C in the urban area, which is much larger than those in the surrounding nonurban areas (Fig. 11a). On the contrary, urbanization causes the mixing ratio to decrease by 0.5-1.8 g kg^{-1} in the urban area (Fig. 11c). This is consistent with previous findings that evaporation in urban area is reduced by impervious surfaces and reduced green vegetation fraction (Guo et al. 2006; Zhang et al. 2009). The model also successfully captures the characteristic of weak wind zones contributed by urbanization (Fig. 11e). The wind speed decreases by 0.3-1.0 m s^{-1} in the urban area due to the drag effect of buildings (i.e., the pressure differences across individual roughness elements). Contrary to changes in mixing ratio, the ensemble study indicates that urban land use lead to an increase in precipitation (Fig.

11g). The differences in the spread of T2M (Fig. 11b), Q2M (Fig.11d), and WS10M (Fig. 11f) are mainly concentrated in the urban area, indicating that the urban land use introduces more uncertainty than natural land use in forecasting the three variables. Considering the magnitude of the ensemble mean, the differences in the spread of precipitation is much larger than those of the other three variables and occur both in and out of the control region. Notably, the distribution characteristics of the differences in the spread of precipitation (Fig. 11h) are similar to those in the ensemble mean (Fig.11g). This illustrates that the ensemble method is quite valuable for assessing the urban impact on local heavy precipitation Buizza 1997().

The individual and combined impacts of thermal and dynamical effects of urbanization are examined by comparing the simulated results of NUB, NTH, and NDY with CTL for three different sets of variables, i.e., thermodynamic variables (i.e., TSK, net radiation (RN), GRDFLX, HFX, and latent heat flux (LH)), dynamical variables (i.e., friction velocity (UST) and turbulent kinetic energy flux (TKEP)), and meteorological variables (i.e., T2M, Q2M, WS10M, and accumulated precipitation). The energy balance in the unban canopy is affected obviously by urbanization, which is represented by an increase in TSK and HFX (Fig.12a1,12d1), and a decrease in RN, GRDFLX, and LH (Fig.12b1, 12c1, and 12e1). A comparison of the results between NTH and NDY (Fig. 12a2-12e2 vs. 12a3-12e3) suggests that changes in these thermodynamic variables are mainly contributed by the thermal effect of urbanization rather than the dynamical effect, which is most likely because the thermal effects of urbanization have a direct impact on the thermal fields in the model. These findings are consistent with previous studies Chen et al. 2016Feng et al. 2012Shen et al. 2019(; ;).

For the dynamical variables, the friction velocity is increased obviously in the downtown of Hangzhou (Fig. 13a1) and is mainly attributed to the dynamical effect of urbanization (Fig. 13a3). It is possibly because the friction velocity is closely related to the roughness length (Fig.10), which is a key variable in calculating the radial and zonal wind in WRF. The numerous high-rise buildings in the downtown make the removal of dynamic effect of urbanization quite sensitive to the changes of surface roughness there. The turbulent kinetic energy (TKE) represents the strength of turbulent mixing in the boundary layer. The TKE is increased obviously in the urban area (Fig. 13b1) and mainly contributed by the thermal effect of urbanization (Fig. 13b2). Zhou and Chen (2018) indicated that the strong thermal turbulence activity caused by urbanization enhanced the transport of momentum flux and the mechanical turbulence, causing an increase in TKE.

The thermal and dynamical effects of urbanization on the last set of variables, i.e., T2M, Q2M, WS10M, and precipitation, are examined and compared in Figure 14. Both the thermal and dynamical effects contribute to an increase in T2M (Fig. 14a1-14a3). The regional averaged values of T2M suggest that the contribution of the thermal effect is slightly larger than that of the dynamical

effect (Fig. 15a). For changes in Q2M, although the dynamical effect is a positive contribution, the thermal effect plays a major role and contributes to a decrease in Q2M (Fig. 14b1-14b3, Fig.15b). The thermal and dynamic effects are also opposite on the changes of wind speed in the urban area (Fig. 14c2 vs. 14c3). However, since the dynamical effect is dominant (Fig. 15c), the WS10M in the urban area is decreased due to urbanization, which is consistent with the difference in WS10M between ENCTL and ENNoUB (Fig. 11e). Similar to T2M, both the thermal and dynamical effects contribute to an increase in precipitation (Fig. 14d1-14d3). For thermal effects, the increase of temperature and thermal turbulence activity promotes the convective motion, which in turn increase precipitation. Also, the dynamical effects could not be ignored. The increased friction velocity and TKE could increase the turbulent mixing strength and then contribute to more precipitation (Fig. 15d).

4 Summary and Conclusions

A typical summer heavy rainfall event occurred in Hangzhou, China, is chosen to analyze the sensitivity of UCPs and the individual and combined impacts of thermal and dynamical effects of urbanization using the integrated WRF/urban modelling system.

The performance of the model is evaluated by using ensemble simulations, which include 24 members with different combinations of physical parameterization schemes. The results show that the WRF model well captures the heavy precipitation and the high temperature, low mixing ratio, and weak wind speed before precipitation. The choices of physical parameterization schemes for simulating precipitation are much more sensitive than those for simulating temperature, mixing ratio, and wind speed before precipitation. The microphysics scheme plays the most important role in simulating precipitation, followed by the PBL, whereas the land surface and urban physics schemes have minimal impacts.

Eight important parameters for characterizing the urban canopy are chosen for investigating their impacts on meteorological variables. The influences of UCPs are mainly concentrated in the urban area, although the effect of UCPs on precipitation is less evenly distributed in space than the other three variables. The temperature, mixing ratio, and precipitation are more sensitive to changes in heat capacity, thermal conductivity, surface albedo, and roughness length. The wind speed is mainly affected by building height, roof width, and road width. Besides, the surface albedo, building height, roof width, and road width play an important role in the urban canopy radiation balance, while the heat capacity and thermal conductivity have a greater influence on the surface energy balance.

The individual and combined impacts of the thermal and dynamic effects of urbanization are also examined. In general, urbanization could lead to higher temperature, less mixing ratio, lower wind speed, and more precipitation in and

around the urban area. Changes in the thermal fields are mainly contributed by the thermal effect of urbanization, while changes in the dynamical fields are mostly determined by the dynamical effect of urbanization. Both the thermal and dynamic effects contribute to an increase in temperature and precipitation and the thermal effect plays a major role. The thermal and dynamic effects are opposite on changes in mixing ratio and wind speed, and they play a major role in each of them respectively.

These results indicate the importance of considering effects of urbanization and various UCPs on numerical weather simulation on both urban and regional scales. However, there are still some limitations to this study. In future studies, more realistic high-resolution UCPs should be used instead of the current default dataset and the influences of the UCPs on atmospheric pollutants should also be considered. In addition, the urban effect on more rainfall events with different synoptic weather backgrounds and long-time climate simulations need to be further analyzed.

Acknowledgments

This study was supported by the National Natural Science Foundation of China (grants 42030610), Science and Technology Project of Zhejiang Province (LGF20D050001, LY21D050001); The Open Grants of the State Key Laboratory of Severe Weather (2021 LASW-B21); Meteorological Science and Technology Project of Zhejiang Meteorological Bureau (2018ZD01, 2019ZD11).

Open Research

Data Availability Statement

The European Centre for Medium-Range Weather Forecasts (ECMWF) reanalysis data (ERA5) used for providing the initial and lateral boundary conditions in this study can be downloaded from the Copernicus' Climate Change Service website (Hersbach et al., 2018). The WRF version 4.0.2 (Software) source codes are obtained from the WRF ARW User's Page supported by Mesoscale and Microscale Meteorology (MMM) Laboratory, National Center for Atmospheric Research (NCAR) (Skamarock et al., 2019).

Appendix. A list of abbreviations

Abbreviations and Descriptions

ALBEDO surface albedo

GLW downward longwave radiation

GLWUP upward longwave radiation

GRDFLX ground heat flux

HFX sensible heat flux

LH latent heat flux

NLW net longwave radiation

NSW net shortwave radiation

PBL planetary boundary layer scheme

PREC precipitation

Q2M 2-m mixing ratio

RMSE root-mean-square error

RN net radiation

SWDOWN downward shortwave radiation

SWUP upward shortwave radiation

TKEP850 turbulent kinetic energy flux at 850 hPa

TS threat score

TSK surface temperature

T2M 2-m temperature

UCP urban canopy parameter

UHI urban heat island

UST friction velocity

WS10M 10-m wind speed

W850 vertical velocity at 850 hPa

Tables

Table 1. Model Configurations

Table 2. Summary of the Numerical Experiments

Table 3. Threat Scores (TS) of accumulated precipitation (from 13:00 to 18:00 BST 26 July 2018) for the Ensemble Study on Different Physical Schemes

Table 4. Biases (BIAS), Root-Mean-Square Errors (RMSE), and Spatial Correlation Coefficients (SCC) of Precipitation (Averaged from 14:00 to 16:00 BST on 26 July 2018), and 2 m temperature, 2 m mixing ratio, and 10 m wind speed before precipitation (Averaged from 09:00 to 13:00 BST on 26 July 2018) for the Ensemble Study on Different Physical Schemes

Table 1. Model Configurations

Model settings	D01
Model and version	WRF v4.0.2
Horizontal grid points	403 × 353
Δx (km)	4
Vertical layers	51
Cumulus physics	None (0)[a]
Shortwave radiation	RRTMG (4) (Iacono et al. 2008)
Longwave radiation	RRTMG (4) (Iacono et al. 2008)
Microphysics	Purdue Lin (2) (Chen and Sun 2002), WSM6 (6) (Hong and Lim 2006), WDM6 (16)
PBL physics	MYJ (2) (Janjić 1994; Mesinger 1993), Boulac (8) (Bougeault and Lacarrere 1989)
Land surface	Noah (2) (Tewari et al. 2016), NoahMP (4) (Niu et al. 2011; Yang et al. 2011)
Urban physics	SLUCM (1) (Chen et al. 2011), BEP (2) (Martilli et al. 2002)

[a]The numbers in parentheses represent the option number for each physical parameterization scheme.

Table 2. Summary of the Numerical Experiments

Group	WRF Simulations	Physical parameterization Options	Notes
GROUP I	ENCTL	Microphysics (Lin(2), WSM6(6), WDM(16)) Planetary Boundary layer (MYJ(2), BouLac(8)) Land Surface (Noah(2), Noahmp(4)) Urban Surface (SLUCM(1), BEP(2))	
	ENNoUB	same as ENCTL	same as ENCTL, but re
GROUP II	CTL	WDM(16)+ BouLac(8)+ Noahmp(4)+ BEP(2)	The control run in ENC
	SEN1 / SEN2	same as CTL	same as CTL, but decre
	SEN3 / SEN4	same as CTL	same as CTL, but decre
	SEN5 / SEN6	same as CTL	same as CTL, but decre
	SEN7 / SEN8	same as CTL	same as CTL, but decre
	SEN9 / SEN10	same as CTL	same as CTL, but decre
	SEN11 / SEN12	same as CTL	same as CTL, but decre
	SEN13 / SEN14	same as CTL	same as CTL, but decre
	SEN15 / SEN16	same as CTL	same as CTL, but decre
GROUP III	CTL	WDM(16)+ BouLac(8)+ Noahmp(4)+ BEP(2)	The control run in ENC
	NOUB	same as CTL	same as CTL, but artifi
	NOTH	same as CTL	same as CTL, but artifi
	NODY	same as CTL	same as CTL, but artifi

Table 3. Threat Scores (TS) of accumulated precipitation (from 13:00 to 18:00 BST on 26 July 2018) for the Ensemble Study on Different Physical Schemes [a]

CASES	TS(0.1mm)	TS(10mm)	TS(25mm)	TS(50mm)
m2p2s2u1	0.87	0.32	0.16	0.02
m2p2s2u2	0.92	0.47	0.27	0.07
m2p2s4u1	0.90	0.41	0.21	0.04
m2p2s4u2	0.93	0.52	0.24	0.07
m2p8s2u1	0.84	0.44	0.19	0.02
m2p8s2u2	0.87	0.43	0.19	0.03
m2p8s4u1	0.82	0.43	0.28	0.16
m2p8s4u2	0.86	0.41	0.19	0.06
m6p2s2u1	0.87	0.34	0.14	0.00
m6p2s2u2	0.88	0.34	0.07	0.00
m6p2s4u1	0.90	0.36	0.16	0.02
m6p2s4u2	0.85	0.37	0.14	0.02
m6p8s2u1	0.86	0.28	0.10	0.11
m6p8s2u2	0.92	0.39	0.14	0.02
m6p8s4u1	0.84	0.43	0.17	0.04
m6p8s4u2	0.84	0.40	0.12	0.00
m16p2s2u1	0.92	0.53	0.26	0.03
m16p2s2u2	0.92	0.48	0.15	0.02
m16p2s4u1	0.90	0.49	0.15	0.02
m16p2s4u2	0.92	0.61	0.34	0.02

CASES	TS(0.1mm)	TS(10mm)	TS(25mm)	TS(50mm)
m16p8s2u1	0.86	0.52	0.20	0.04
m16p8s2u2	0.93	0.53	0.19	0.02
m16p8s4u1	0.90	0.60	0.30	0.15
m16p8s4u2	0.92	0.56	0.33	0.07
Mean	0.87	0.37	0.14	0.03

[a]The colored grid points are the top 25% members, the darker the color, the higher the model performance.

Table 4. The ensemble means and variations of Biases (BIAS) and Root-Mean-Square Errors (RMSE) of 2 m Temperature, 2 m Mixing ratio, and 10 m Wind Speed before Precipitation (Averaged from 10:00 to 13:00 BST on 26 July 2018), and Precipitation (accumulated from 13:00 to 18:00 BST on 26 July 2018) for the Ensemble Study on Different Physical Schemes

Variables	Scores	Ensemble Mean	Ensemble Variation
T2M	BIAS(°C)	-1.43	0.27
	RMSE(°C)	1.97	0.16
Q2M	BIAS(k kg^{-1})	-1.83	0.42
	RMSE(k kg^{-1})	2.54	0.20
WS10M	BIAS(m s^{-1})	1.31	0.13
	RMSE(m s^{-1})	1.73	0.09
PREC	BIAS(mm)	-6.14	13.64
	RMSE(mm)	29.08	2.22

Figures

Figure 1. The ERA5 reanalysis of geopotential height at 500-hPa (solid lines), wind speed (arrow), and relative humidity (shading) at 850-hPa averaged from 09:00 to 18:00 on 26 July, 2018. The black dot indicates the location of Hangzhou.

Figure 2. The (a) simulated domain d01 with terrain (m) and (b) land use in domain d02. The black rectangle box (119.9-120.8 °E, 29.8-30.7 °N) represents the control region of this heavy rain event. The magenta solid line in (b) indicates the Hangzhou-Shaoxing mega city with urban fraction 0.2.

Figure 3. Comparison of the (a1-d1) observed and (a2-d2) simulated composite radar reflectivity (dBZ) at 4 selected times on 26 July 2018. Note an approximate shift of 1.5 h between the simulation and observation.

Figure 4. Distribution of the 2-m temperature (℃) averaged during 10:00 to 13:00 BST on 26 July 2018: (a1) observation, (b1) ensemble mean, (c1) CTL

run, and (d1) spread. (a2-d2) the same as (a1-d1) but for the 2-m mixing ratio (g kg-1); (a3-d3) the same as (a1-d1) but for the 10-m wind (m s-1); (a4-d4) similar to (a1-d1) but for the accumulated precipitation (mm) during 13:00 to 18:00 BST on 26 July 2018.

Figure 5. Time series of the (a) 2-m temperature (℃), (b) 2-m mixing ratio (g kg^{-1}), (c) 10-m wind speed (m s^{-1}), and (d) precipitation (mm) averaged over the control region from 08:00 to 20:00 BST on 26 July 2018. The red line denotes observation, the gray lines are the 24 ensemble members, and the blue line represents the ensemble mean.

Figure 6. The temperature differences (℃) at 10:00 BST on 26 July 2018 between the 16 sensitivity tests in GROUP II (i.e., SEN1, SEN2, …, SEN16) and the CTL (m16p8s4u2) by: (a) decreasing the building height; (b) increasing the building height; (c) decreasing the roof width; (d) increasing the roof width; (e) decreasing the road width; (f) increasing the road width; (g) decreasing the anthropogenic heat; (h) increasing the anthropogenic heat; (i) decreasing the heat capacity; (j) increasing the heat capacity; (k) decreasing the thermal conductivity; (l) increasing the thermal conductivity; (m) decreasing the surface albedo; (n) increasing the surface albedo; (o) decreasing the roughness length; (p) increasing the roughness length by 50%, respectively.

Figure 7. The same as Figure 6, but for the 2-m mixing ratio (g kg^{-1}).

Figure 8. The same as Figure 6, but for the 10-m wind speed (m s^{-1}).

Figure 9. The same as Figure 6, but for 1-hr accumulated precipitation (mm) during 13:00-14:00 BST on 26 July 2018.

Figure 10. Difference in multiple meteorological variable averaged in the control region caused by increasing urban canopy parameters by 50% in each sensitivity test (i.e., SEN1, SEN2, …, SEN16). The colored grid points are the four most changed members in each column, the darker the color, the greater the absolute value. TSK – surface temperature, T2M – 2-m temperature, Q2M – 2-m mixing ratio, WS10M – 10-m wind speed, PREC – precipitation, ALBEDO – surface albedo, SWDOWN – downward shortwave radiation, SWUP – upward shortwave radiation, NSW – net shortwave radiation, GLW – downward longwave radiation, GLWUP – upward longwave radiation, NLW – net longwave radiation, RN – net radiation, LH – latent heat flux, HFX – sensible heat flux, GRDFLX—ground heat flux, UST – friction velocity, TKEP - turbulent kinetic energy flux at 850 hPa, W850 – vertical velocity at 850 hPa.

Figure 11. Differences between ENCTL and ENNoUB in ensemble mean (left) and spread (right) of (a, b) 2-m temperature (℃) and (c, d) 2-m mixing ratio (g kg^{-1}) during 10:00 to 13:00 BST on 26 July 2018, and (e, f) 10-m wind speed (m s^{-1}) and (g, h) accumulated precipitation (mm) during 10:00 to 18:00 BST on 26 July 2018.

Figure 12. Differences of (a1-a3) surface skin temperature (℃), (b1-b3) surface net radiation (W m^{-1}), (c1-c3) ground head flux (W m^{-1}), (d1-d3) sensible heat

flux (W m^{-1}), and (e1-e3) latent heat flux (W m^{-1}) averaged during 10:00 to 13:00 BST on 26 July 2018 between the control test (CTL) and (left) NoUB, (middle) NoTH, and (right) NoDY test.

Figure 13. Same as Figure 12, but for (a1-a3) friction velocity UST (m s^{-1}), and (b1-b3) turbulent kinetic energy TKEP (m^2 s^{-2}) at 850h Pa during 10:00 to 18:00 BST on 26 July 2018.

Figure 14. Same as Figure 12, but for (a1-a3) 2-m temperature (℃) and (b1-b3) 2-m mixing ratio (g kg^{-1}) during 10:00 to 13:00 BST on 26 July 2018, and (c1-c3) 10-m wind speed (m s^{-1}) and (d1-d3) accumulated precipitation (mm) during 10:00 to 18:00 BST on 26 July 2018.

Figure 15. Comparison of the impacts of the total, thermal, and dynamic effects of urbanization on (a) 2-m temperature (℃) and (b) 2-m mixing ratio (g kg^{-1}) averaged during 10:00 to 13:00 BST on 26 July 2018, and (c) 10-m wind speed (m s^{-1}) and (d) accumulated precipitation (mm) averaged during 10:00 to 18:00 BST on 26 July 2018 .

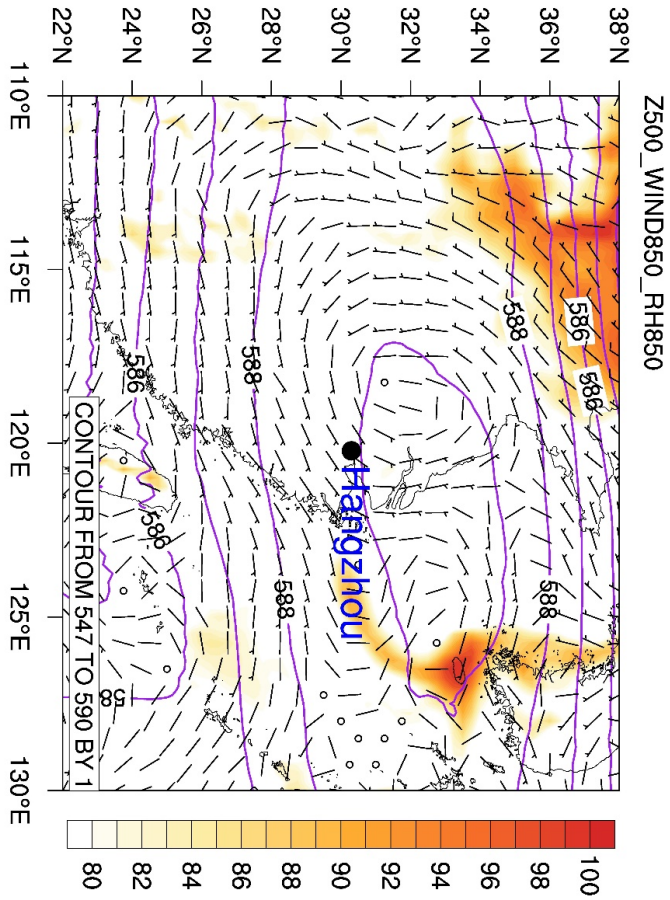

Figure 1. The ERA5 reanalysis of geopotential height at 500-hPa (solid lines), wind speed (arrow), and relative humidity (shading) at 850-hPa averaged from 09:00 to 18:00 on 26 July, 2018. The black dot indicates the location of Hangzhou.

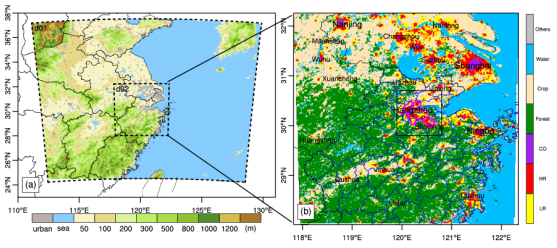

Figure 2. The (a) simulated domain d01 with terrain (m) and (b) land use in domain d02. The black rectangle box (119.9-120.8 °E, 29.8-30.7 °N) represents the control region of this heavy rain event. The magenta solid line in (b) indicates the Hangzhou-Shaoxing mega city with urban fraction 0.2.

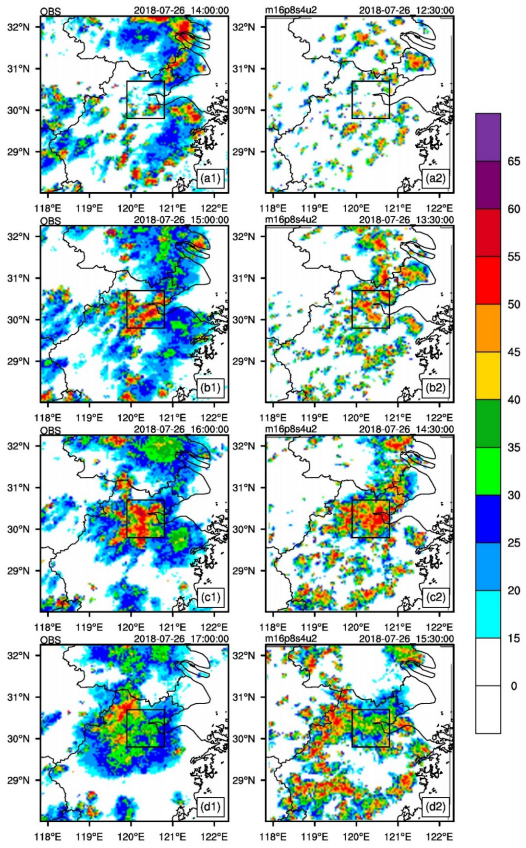

Figure 3. Comparison of the (a1-d1) observed and (a2-d2) simulated composite radar reflectivity (dBZ) at 4 selected times on 26 July 2018. Note an approximate shift of 1.5 h between the simulation and observation.

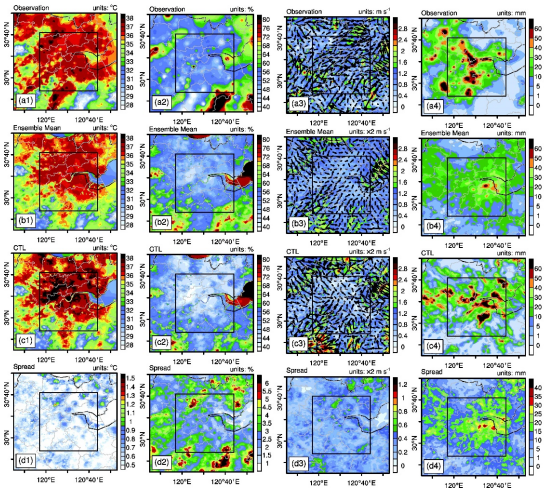

Figure 4. Distribution of the 2-m temperature (℃) averaged during 10:00 to 13:00 BST on 26 July 2018: (a1) observation, (b1) ensemble mean, (c1) CTL run, and (d1) spread. (a2-d2) the same as (a1-d1) but for the 2-m mixing ratio (g kg^{-1}); (a3-d3) the same as (a1-d1) but for the 10-m wind (m s^{-1}); (a4-d4) similar to (a1-d1) but for the accumulated precipitation (mm) during 13:00 to 18:00 BST on 26 July 2018.

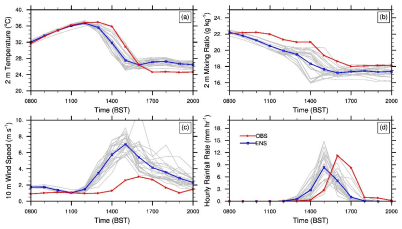

Figure 5. Time series of the (a) 2-m temperature (℃), (b) 2-m mixing ratio (g kg^{-1}), (c) 10-m wind speed (m s^{-1}), and (d) precipitation (mm) averaged over the control region from 08:00 to 20:00 BST on 26 July 2018. The red line denotes observation, the gray lines are the 24 ensemble members, and the blue line represents the ensemble mean.

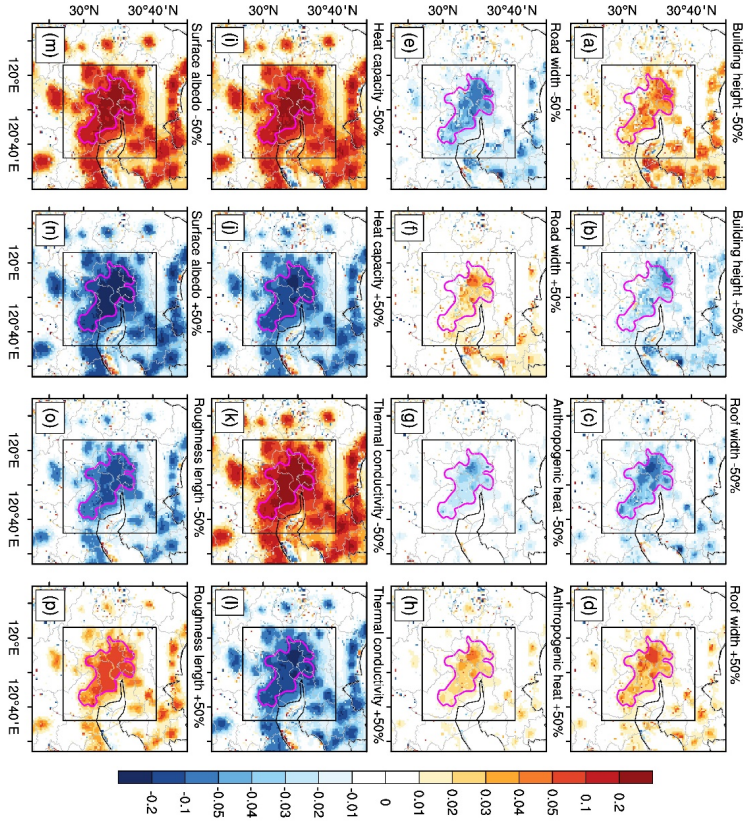

Figure 6. The temperature differences (℃) at 10:00 BST on 26 July 2018 between the 16 sensitivity tests in GROUP II (i.e., SEN1, SEN2, ..., SEN16) and the CTL (m16p8s4u2) by: (a) decreasing the building height; (b) increasing the building height; (c) decreasing the roof width; (d) increasing the roof width; (e) decreasing the road width; (f) increasing the road width; (g) decreasing the anthropogenic heat; (h) increasing the anthropogenic heat; (i) decreasing the heat capacity; (j) increasing the heat capacity; (k) decreasing the thermal conductivity; (l) increasing the thermal conductivity; (m) decreasing the surface albedo; (n) increasing the surface albedo; (o) decreasing the roughness length; (p) increasing the roughness length by 50%, respectively.

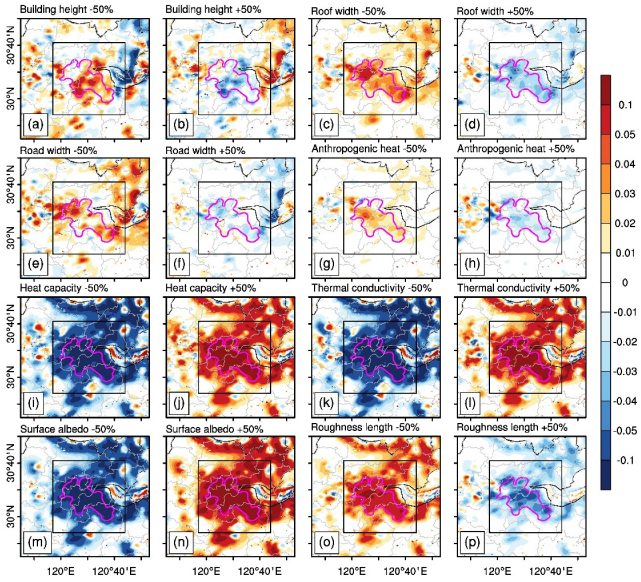

Figure 7. The same as Figure 6, but for the 2-m mixing ratio (g kg^{-1}).

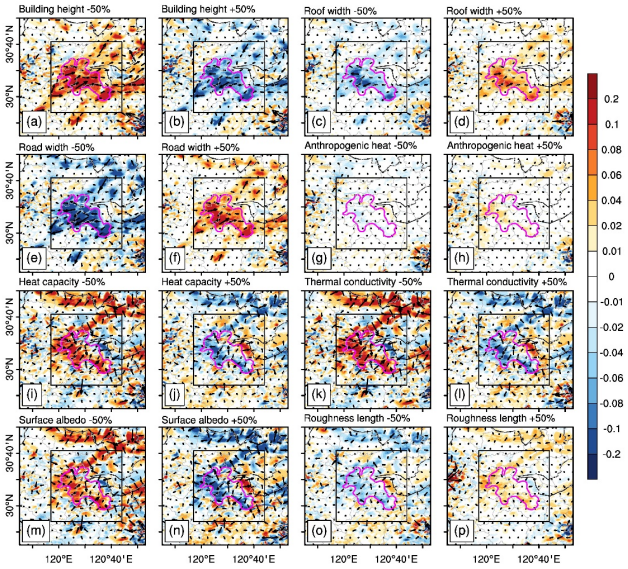

Figure 8. The same as Figure 6, but for the 10-m wind speed (m s^{-1}).

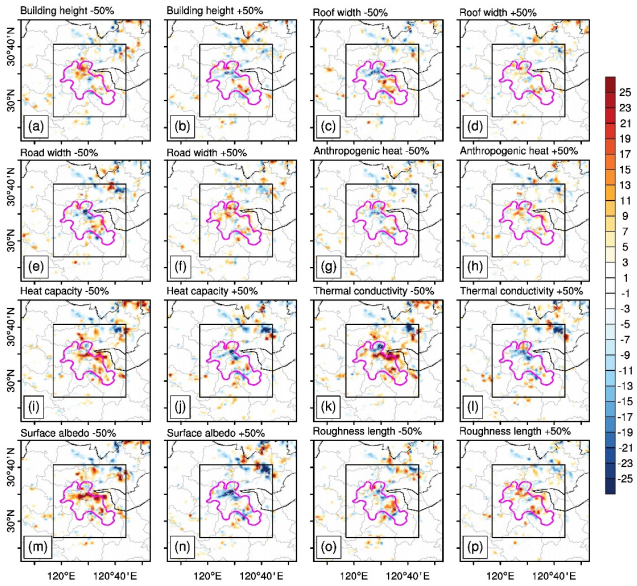

Figure 9. The same as Figure 6, but for 1-hr accumulated precipitation (mm) during 13:00-14:00 BST on 26 July 2018.

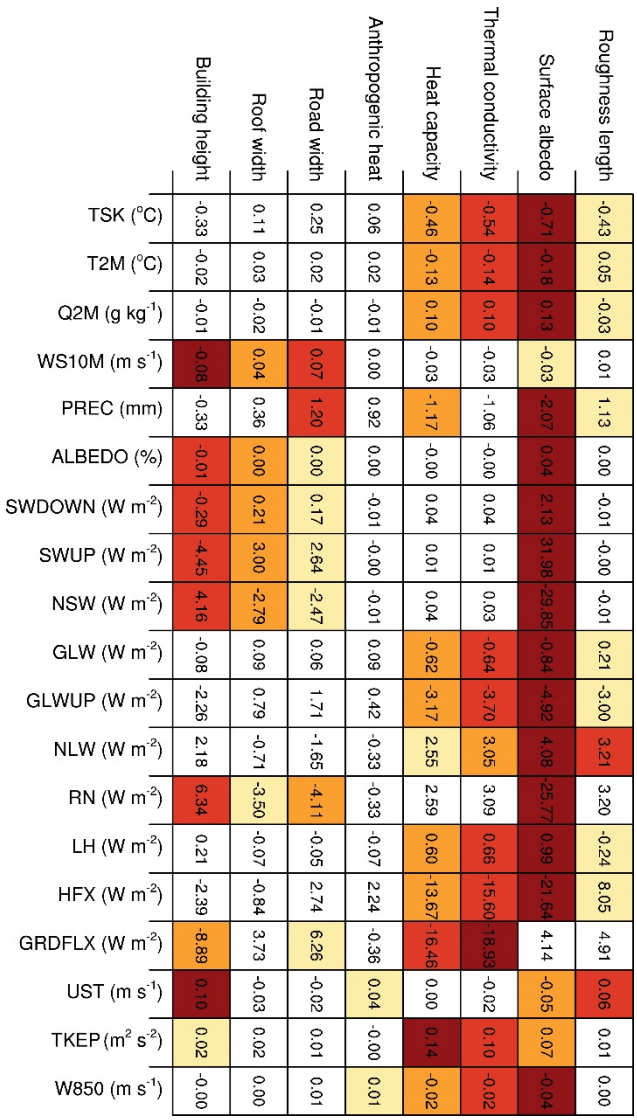

Figure 10. Difference in multiple meteorological variable averaged in the control region caused by increasing urban canopy parameters by 50% in each sensitivity test (i.e., SEN1, SEN2, ..., SEN16). The colored grid points are the four most changed members in each column, the darker the color, the greater the absolute value. TSK – surface temperature, T2M – 2-m temperature, Q2M – 2-m mixing ratio, WS10M – 10-m wind speed, PREC – precipitation, ALBEDO – surface albedo, SWDOWN – downward shortwave radiation, SWUP – upward shortwave radiation, NSW – net shortwave radiation, GLW – downward longwave radiation, GLWUP – upward longwave radiation, NLW – net longwave radiation, RN – net radiation, LH – latent heat flux, HFX – sensible heat flux,

GRDFLX—ground heat flux, UST – friction velocity, TKEP - turbulent kinetic energy flux at 850 hPa, W850 – vertical velocity at 850 hPa.

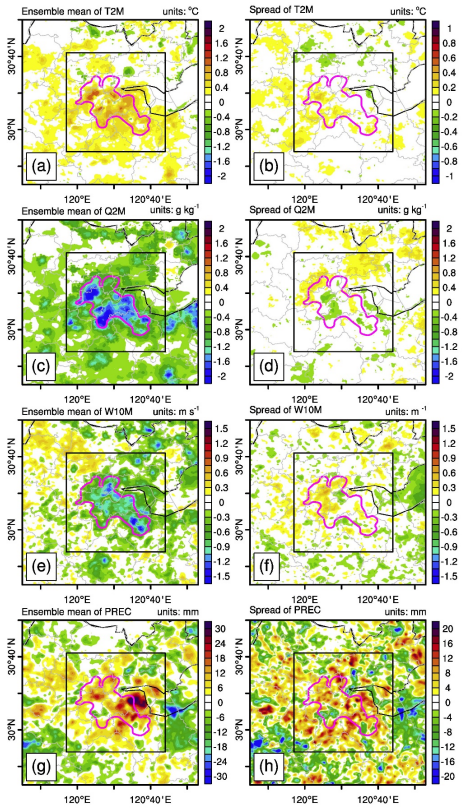

Figure 11. Differences between ENCTL and ENNoUB in ensemble mean (left) and spread (right) of (a, b) 2-m temperature (℃) and (c, d) 2-m mixing ratio (g kg^{-1}) during 10:00 to 13:00 BST on 26 July 2018, and (e, f) 10-m wind speed (m s^{-1}) and (g, h) accumulated precipitation (mm) during 10:00 to 18:00 BST on 26 July 2018.

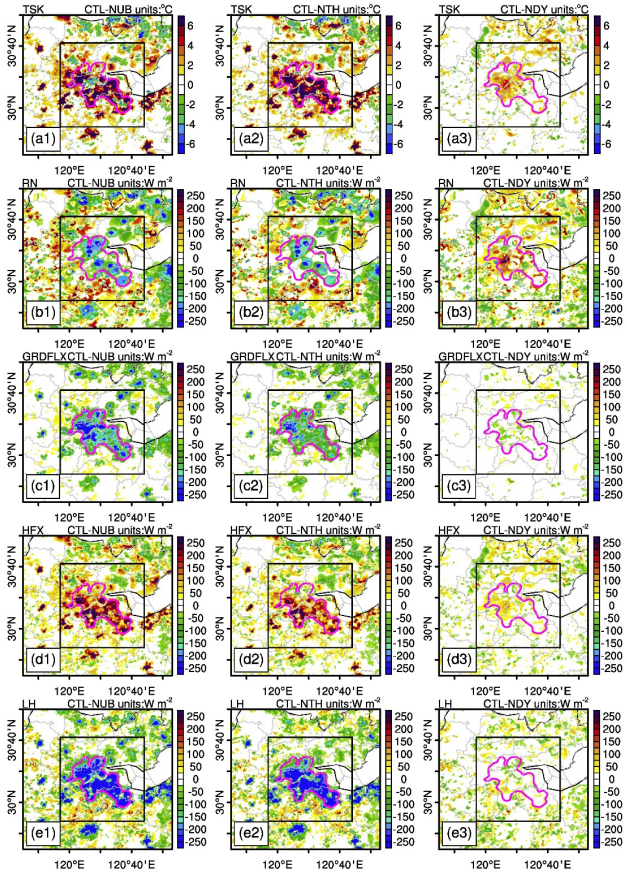

Figure 12. Differences of (a1-a3) surface skin temperature (℃), (b1-b3) surface net radiation (W m^{-1}), (c1-c3) ground head flux (W m^{-1}), (d1-d3) sensible heat flux (W m^{-1}), and (e1-e3) latent heat flux (W m^{-1}) averaged during 10:00 to 13:00 BST on 26 July 2018 between the control test (CTL) and (left) NoUB, (middle) NoTH, and (right) NoDY test.

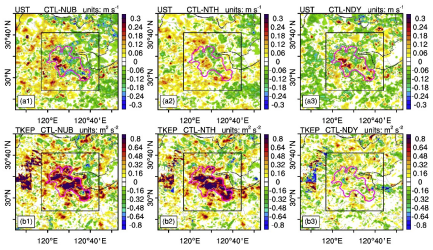

Figure 13. Same as Figure 12, but for (a1-a3) friction velocity UST (m s^{-1}), and (b1-b3) turbulent kinetic energy TKEP (m^2 s^{-2}) at 850h Pa during 10:00 to 18:00 BST on 26 July 2018.

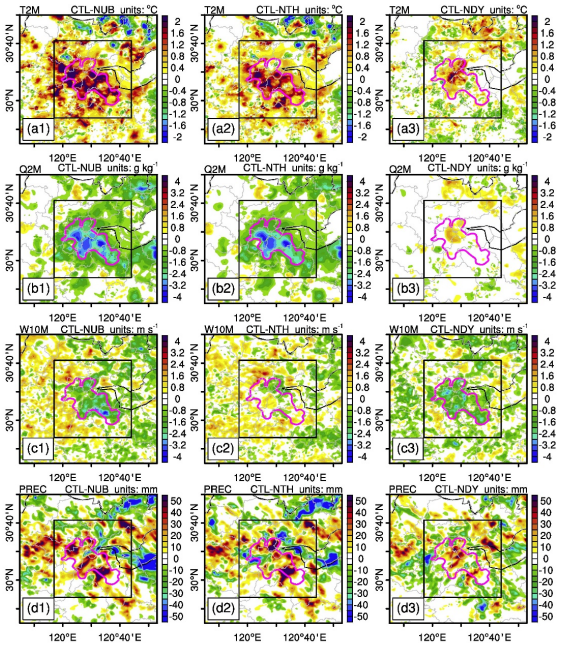

Figure 14. Same as Figure 12, but for (a1-a3) 2-m temperature (℃) and (b1-b3) 2-m mixing ratio (g kg^{-1}) during 10:00 to 13:00 BST on 26 July 2018, and (c1-c3) 10-m wind speed (m s^{-1}) and (d1-d3) accumulated precipitation (mm) during 10:00 to 18:00 BST on 26 July 2018.

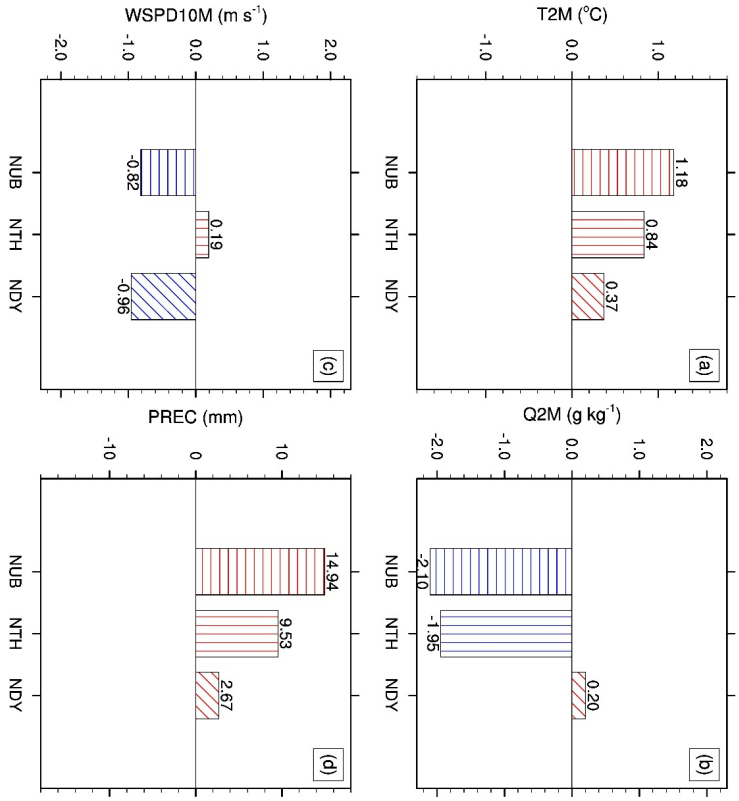

Figure 15. Comparison of the impacts of the total, thermal, and dynamic effects of urbanization on (a) 2-m temperature (℃) and (b) 2-m mixing ratio (g kg^{-1}) averaged during 10:00 to 13:00 BST on 26 July 2018, and (c) 10-m wind speed (m s^{-1}) and (d) accumulated precipitation (mm) averaged during 10:00 to 18:00 BST on 26 July 2018 .

References

Akbari, H., S. Davis, J. Huang, S. Dorsano, and S. Winnett, 1992: Cooling our communities: A guidebook on tree planting and light-colored surfacing,

Medium: ED; Size: Pages: (220 p) pp.Bougeault, P., and P. Lacarrere, 1989: Parameterization of Orography-Induced Turbulence in a Mesobeta-Scale Model. *Monthly Weather Review*, **117,** 1872-1890.Buizza, 1997: Potential Forecast Skill of Ensemble Prediction and Spread and Skill Distributions of the ECMWF Ensemble Prediction System. *Monthly Weather Review*, **125,** 99-119.Chen, F., X. Yang, and W. Zhu, 2014: WRF simulations of urban heat island under hot-weather synoptic conditions: The case study of Hangzhou City, China. *Atmospheric Research*, **138,** 364-377.Chen, F., X. Yang, and J. Wu, 2016: Simulation of the urban climate in a Chinese megacity with spatially heterogeneous anthropogenic heat data. *Journal of Geophysical Research: Atmospheres*, **121,** 5193-5212.Chen, F., M. Wu, M. Dong, and B. Yu, 2022a: Comparison of the Impacts of Topography and Urbanization on an Extreme Rainfall Event in the Hangzhou Bay Region. *Journal of Geophysical Research: Atmospheres*, **127,** e2022JD037060.Chen, F., B. Yu, M. Wu, and X. Yang, 2022b: Improved Urban Finescale Forecasting During a Heat Wave by Using High-Resolution Urban Canopy Parameters. *Frontiers in Climate*, **3**.Chen, F., and Coauthors, 2011: The integrated WRF/urban modelling system: development, evaluation, and applications to urban environmental problems. *International Journal of Climatology*, **31,** 273-288.Chen, L., and E. Ng, 2011: Quantitative urban climate mapping based on a geographical database: A simulation approach using Hong Kong as a case study. *International Journal of Applied Earth Observation and Geoinformation*, **13,** 586-594.Chen, S., and W. Sun, 2002: A One-dimensional Time Dependent Cloud Model. *Journal of the Meteorological Society of Japan. Ser. II*, **80,** 99-118.Chen, Y., and W. Jiang, 2006: The numerical experiments of the effect of urban buildings on boundary layer structure. *Plateau Meteorology (in Chinese)*, **25,** 824-833.Ching, J., and Coauthors, 2009: National Urban Database and Access Portal Tool. *Bulletin of the American Meteorological Society*, **90,** 1157-1168.Coutts, A. M., E. Daly, J. Beringer, and N. J. Tapper, 2013: Assessing practical measures to reduce urban heat: Green and cool roofs. *Building and Environment*, **70,** 266-276.Feng, J., Y. Wang, Z. Ma, and Y. Liu, 2012: Simulating the Regional Impacts of Urbanization and Anthropogenic Heat Release on Climate across China. *Journal of Climate*, **25,** 7187-7203.He, X., Y. Li, X. Wang, L. Chen, B. Yu, Y. Zhang, and S. Miao, 2019: High-resolution dataset of urban canopy parameters for Beijing and its application to the integrated WRF/Urban modelling system. *Journal of Cleaner Production*, **208,** 373-383.Hersbach, H., and Coauthors, 2018: ERA5 hourly data on pressure levels from 1979 to present. *Copernicus Climate Change Service (C3S) Climate Data Store (CDS)*.Hong, S. Y., and J. O. Lim, 2006: The WRF single-moment 6-class microphysics scheme (WSM6). *J. Korean Meteor. Soc.*, **42,** 129-151.Huang, Y., Y. Liu, Y. Liu, H. Li, and J. Knievel, 2019: Mechanisms for a Record-Breaking Rainfall in the Coastal Metropolitan City of Guangzhou, China: Observation Analysis and Nested Very Large Eddy Simulation With the WRF Model. *Journal of Geophysical Research Atmospheres*, **124**.Iacono, M. J., J. S. Delamere, E. J. Mlawer, M. W. Shephard, S. A. Clough, and W. D. Collins, 2008: Radiative forcing by long-lived greenhouse gases: Calculations with the AER radiative transfer models. *Journal of Geophysical Research: Atmospheres*,

113, D13103.Ikeda, K., and Coauthors, 2010: Simulation of seasonal snowfall over Colorado. *Atmospheric Research*, **97,** 462-477.Janjić, Z. I., 1994: The Step-Mountain Eta Coordinate Model: Further Developments of the Convection, Viscous Sublayer, and Turbulence Closure Schemes. *Monthly Weather Review*, **122,** 927-945.Jiang, X., Y. Luo, D.-L. Zhang, and M. Wu, 2020: Urbanization Enhanced Summertime Extreme Hourly Precipitation over the Yangtze River Delta. *Journal of Climate*, **33,** 5809-5826.Kusaka, H., and F. Kimura, 2004: Coupling a single-layer urban canopy model with a simple atmospheric model: Impact on urban heat island simulation for an idealized case. *Journal of the Meteorological Society of Japan*, **82,** 67-80.Kusaka, H., H. Kondo, Y. Kikegawa, and F. Kimura, 2001: A simple single-layer urban canopy model for atmospheric models: Comparison with multi-layer and slab models. *Boundary-Layer Meteorology*, **101,** 329-358.Lim, K.-S. S., and S.-Y. Hong, 2010: Development of an Effective Double-Moment Cloud Microphysics Scheme with Prognostic Cloud Condensation Nuclei (CCN) for Weather and Climate Models. *Monthly Weather Review*, **138,** 1587-1612.Liu, X., G. Tian, J. Feng, J. Wang, and L. Kong, 2018: Assessing summertime urban warming and the cooling efficacy of adaptation strategy in the Chengdu-Chongqing metropolitan region of China. *Science of The Total Environment*, **610-611,** 1092-1102.Liu, Y., F. Chen, T. Warner, and J. Basara, 2006: Verification of a mesoscale data-assimilation and forecasting system for the Oklahoma City area during the Joint Urban 2003 field project. *Journal of Applied Meteorology and Climatology*, **45,** 912-929.Martilli, A., 2007: Current research and future challenges in urban mesoscale modelling. *International Journal of Climatology*, **27,** 1909-1918.Martilli, A., A. Clappier, and M. W. Rotach, 2002: An urban surface exchange parameterisation for mesoscale models. *Boundary-Layer Meteorology*, **104,** 261-304.Mesinger, F., 1993: Forecasting upper tropospheric turbulence within the framework of the Mellor-Yamada 2.5 closure. CAS/JSC WGNE 18, 4.28-24.29 pp.Miao, S., F. Chen, M. A. LeMone, M. Tewari, Q. Li, and Y. Wang, 2009: An Observational and Modeling Study of Characteristics of Urban Heat Island and Boundary Layer Structures in Beijing. *Journal of Applied Meteorology and Climatology*, **48,** 484-501.Miao, Y., S. Liu, Y. Zheng, S. Wang, and B. Chen, 2015: Numerical Study of the Effects of Topography and Urbanization on the Local Atmospheric Circulations over the Beijing-Tianjin-Hebei, China. *Advances in Meteorology*, **2015,** 1-16.Millstein, D., and S. Menon, 2011: Regional climate consequences of large-scale cool roof and photovoltaic array deployment. *Environmental Research Letters*, **6,** 034001.Mittal, H., A. Sharma, and A. Gairola, 2018: A review on the study of urban wind at the pedestrian level around buildings. *Journal of Building Engineering*, **18,** 154-163.Niu, G., and Coauthors, 2011: The community Noah land surface model with multiparameterization options (Noah-MP): 1. Model description and evaluation with local-scale measurements. *Journal of Geophysical Research*, **116,** D12109.Portman, D. A., 1993: Identifying and Correcting Urban Bias in Regional Time Series: Surface Temperature in China's Northern Plains. *Journal of Climate*, **6,** 2298-2308.Ren, G. Y., Y. Q. Zhou, Z. Y. Chu, J. X. Zhou, A. Y. Zhang, J. Guo, and X. F. Liu, 2008: Urbanization effects on observed surface air temperature trends in north China. *JOURNAL OF*

CLIMATE, **21,** 1333-1348.Ronda, R. J., G. J. Steeneveld, B. G. Heusinkveld, J. J. Attema, and A. A. M. Holtslag, 2017: Urban Finescale Forecasting Reveals Weather Conditions with Unprecedented Detail. *Bulletin of the American Meteorological Society*, **98,** 2675-2688.Shen, C., and Coauthors, 2019: Impacts of High-Resolution Urban Canopy Parameters within the WRF Model on Dynamical and Thermal Fields over Guangzhou, China. *Journal of Applied Meteorology and Climatology*, **58,** 1155-1176.Shui, T., J. Liu, P. Zhang, S. Liu, and Z. Zhao, 2016: Development of an urban canopy model for the evaluation of urban thermal climate with snow cover in severe cold regions. *Building and Environment*, **95,** 160-170.Skamarock, W. C., and Coauthors, 2019: A Description of the Advanced Research WRF Version 4. NCAR Tech. Note NCAR/TN-556+STR, 145 pp.Smith, K. R., and P. J. Roebber, 2011: Green Roof Mitigation Potential for a Proxy Future Climate Scenario in Chicago, Illinois. *Journal of Applied Meteorology and Climatology*, **50,** 507.Strahler, A., 1999: MODIS Land Cover Product Algorithm Theoretical Basis Document (ATBD) Version 5.0. Technical Report, 72 pp.Sun, Y., N. Zhang, S. Miao, F. Kong, Y. Zhang, and N. Li, 2021: Urban Morphological Parameters of the Main Cities in China and Their Application in the WRF Model. *Journal of Advances in Modeling Earth Systems*, **13**.Tewari, M., and Coauthors, 2016: Implementation and verification of the united NOAH land surface model in the WRF model. *20th Conference on Weather Analysis and Forecasting/16th Conference on Numerical Weather Prediction*, 11-15.Wang, X., and Y. Gong, 2010: The impact of an urban dry island on the summer heat wave and sultry weather in Beijing City. *Chinese Science Bulletin*, **55,** 1657-1661.Wang, X., W. S. Lin, L. Yang, R. R. Deng, and H. Lin, 2007: A numerical study of influences of urban land-use change on ozone distribution over the Pearl River Delta Region, China. *Tellus B*, **59,** 633-641.Wen, J., J. Chen, W. Lin, B. Jiang, S. Xu, and J. Lan, 2020: Impacts of Anthropogenic Heat Flux and Urban Land-Use Change on Frontal Rainfall near Coastal Regions: A Case Study of a Rainstorm over the Pearl River Delta, South China. *Journal of Applied Meteorology and Climatology*, **59,** 363-379.Xu, L., M. Dong, and F. Chen, 2017: Comparison study of spatial interpolation methods based on hourly precipitation data from automatic weather stations. *Journal of Meteorology and Environment (in Chinese)*, **33,** 34-43.Yang, X., Y. Hou, and B. Chen, 2011a: Observed surface warming induced by urbanization in east China. *Journal of Geophysical Research: Atmospheres*, **116**.Yang, X., F. Chen, W. Zhu, and W. Teng, 2015: Urbanization effects on observed changes in summer extreme heat events over Zhejiang Province, east China. *Journal of Tropical Meteorology*, **21,** 295-302.Yang, Z., and Coauthors, 2011b: The community Noah land surface model with multiparameterization options (Noah-MP): 2. Evaluation over global river basins. *Journal of Geophysical Research: Atmospheres*, **116,** D12110.Yin, J., D.-L. Zhang, Y. Luo, and R. Ma, 2020: On the Extreme Rainfall Event of 7 May 2017 over the Coastal City of Guangzhou. Part I: Impacts of Urbanization and Orography. *Monthly Weather Review*, **148,** 955-979.Yu, M., S. Miao, and H. Zhang, 2018: Uncertainties in the Impact of Urbanization on Heavy Rainfall: Case Study of a Rainfall Event in Beijing on 7 August 2015. *Journal of Geophysical Research: Atmospheres*,

123, 6005-6021.Zhang, C. L., F. Chen, S. G. Miao, Q. C. Li, X. A. Xia, and C. Y. Xuan, 2009: Impacts of urban expansion and future green planting on summer precipitation in the Beijing metropolitan area. *Journal of Geophysical Research: Atmospheres*, **114**.Zhang, H., S. Wang, J. Hao, X. Wang, S. Wang, F. Chai, and M. Li, 2016: Air pollution and control action in Beijing. *Journal of Cleaner Production*, **112,** 1519-1527.Zhou, X., and H. Chen, 2018: Impact of urbanization-related land use land cover changes and urban morphology changes on the urban heat island phenomenon. *Science of The Total Environment*, **635,** 1467-1476.